

Observation of Quantum Criticality Class Crossover at the LaAlO₃/KTaO₃ (111) Interface

Jia Liu,^{1,*} Long Cheng,^{1,*†} Junkun Zha,^{1,2} Fei Ye,¹ Xiaofang Zhai^{1,†}

¹ School of Physical Science and Technology, Shanghai Tech University, Pudong, Shanghai 201210, China.

² Department of Physics, University of Science and Technology of China, Hefei, Anhui 230026, China

* These authors contributed equally to this work.

† Corresponding authors: chenglong1@shanghaitech.edu.cn,
zhaxf@shanghaitech.edu.cn.

Abstract

In two-dimensional (2D) limit, the quantum fluctuation is significantly enhanced which could induce a quantum phase transition. Investigating the quantum criticality is an effective approach to elucidate the underlying physics of 2D superconductivity. Here we report the observation of different universality classes of quantum criticality at the superconducting LaAlO₃/KTaO₃ (111) interface, i.e. the normal quantum Griffiths singularity (QGS) and the anomalous QGS. The switch of the quantum criticality class is observed from the normal QGS in a low T_c sample with weaker spin-orbit coupling (SOC) to the anomalous QGS in a high T_c sample with stronger SOC. Moreover, owing to the remarkable SOC strength, the high T_c sample exhibits an unprecedentedly enhanced quantum fluctuation at an unusually elevated temperature approaching the Berezinskii-Kosterlitz-Thouless (BKT) transition temperature T_{BKT} . This work provides comprehensive recognition of the different quantum criticality classes in the same superconducting LaAlO₃/KTaO₃ (111) system, which deepens the understanding of the superconducting mechanism of interfacial superconductors.

Introduction

The 2D superconductivity has recently emerged as the new frontier of discovering exotic physical phenomena, such as the Majorana fermion [1], the quantum bosonic metal [2,3], the Higgs mode [4,5], etc. In 2D limit, the pronounced quantum fluctuation can induce quantum phase transitions and tailor the phase boundary by mutual interplay with thermal fluctuations, disorders, etc. In realistic superconducting materials, quenched disorder is inevitable, which could enhance the quantum fluctuation by formation of superconducting rare regions [6]. In 2D superconductors, quenched disorder leads to the divergent dynamical critical exponent towards zero temperature, which has been theoretically predicted as QGS [7]. Recently, QGS has been experimentally confirmed in many 2D disordered superconductors [6,8-13].

In transitional metal oxides (TMOs), competition and coupling of multiple degrees of freedom constitute the background of many exotic phenomena. For example, in high T_c cuprates, competition between magnetism and superconducting is considered key to the mechanism behind the unconventional superconductivity [14]. Investigating the pair-forming/breaking characters near the quantum phase transition has become an important path to achieve insights on the superconducting mechanism in high T_c cuprates [15,16] and other superconducting systems [17,18]. The superconducting two-dimensional electron gas (2DEG) at oxide interfaces, represented by the well-known $\text{LaAlO}_3/\text{SrTiO}_3$ system [19,20], is a distinct family of superconductors belonging to both TMO and 2D superconductor communities. Recently, the KTaO_3 -based 2DEG [21,22] has been found to have almost one order-of-magnitude higher T_c (~ 2 K) than the $\text{LaAlO}_3/\text{SrTiO}_3$ (~ 300 mK). In both systems, defects such as oxygen vacancies and metal substitutions not only serve as the carrier donors but also act as the quenched disorders [21], which obscures the superconducting mechanism. Furthermore, the

inversion symmetry breaking at the interface promises the giant SOC, which induces mixed spin singlet and triplet pairing channels [23,24]. So far, the mechanism responsible for the KTaO₃ interfacial superconductivity is still under intensive study [21,22,24-27]. It is tempting to investigate the quantum phase transition in order to find out roles of different degrees of freedom, such as SOC, in manipulating the KTaO₃-based superconductivity.

Here we systematically study the quantum criticality of the superconducting 2DEG at the LaAlO₃/KTaO₃ (111) interface. The LaAlO₃/KTaO₃ samples with different T_c were fabricated by pulsed laser deposition with varied growth conditions. Based on the thorough low temperature transport measurements, we reveal that both the T_c and SOC increase with the strength of the disorder scattering. More strikingly, we observe a switch between two different universality classes of the superconducting quantum criticality. Specifically, the low T_c sample with weak SOC shows a normal-like QGS behavior, featuring the enhanced critical magnetic field near zero temperature. On the contrary, the high T_c sample with strong SOC exhibits a rarely-seen anomalous QGS, which presents a maximal critical field near the T_{BKT} and an outward-buckled phase boundary. Our observations provide strong evidence that the intertwined strong SOC and high degree of disorder are intimately connected to the enhanced superconductivity with extremely strong quantum fluctuation.

Results

The LaAlO₃/KTaO₃ heterostructures were fabricated by growing LaAlO₃ overlayers on KTaO₃ (111) substrates using pulsed laser deposition. We achieved samples of different superconducting transition temperatures by controlling the growth temperature. Hall bar geometry was adopted for electrical transport measurements, as

schematically shown in Fig. 1(a). More details of sample preparation and transport measurements are described in Supplemental Material Methods. The temperature dependent resistances under zero field of two representative samples with the highest and lowest T_c are shown in Fig. 1(b). The T_c^{zero} is 1.81 K and 1.27 K, and the T_c defined at the half resistance of the normal state is 2.08 K and 1.43 K for the two samples respectively. The T_{BKT} is also estimated with the power law $V \propto I^\alpha$ ($\alpha = 3$) behavior from the temperature-dependent I - V curves, which turns out to be 1.88 K for the high T_c sample and 1.27 K for the low T_c sample in Fig. S1. The T_{BKT} is close to the T_c^{zero} for both samples.

The residual sheet resistance at 10 K is 3693 Ω/\square for high T_c sample and 2037 Ω/\square for the low T_c one. The larger residual sheet resistance implies the enhanced disorder-induced scattering of carriers. Meanwhile, the high T_c sample shows a lower residual resistance ratio (RRR) and a lower $k_F l$ value with k_F being the Fermi wave vector and l being the mean free path in Fig. S2 and Table S1. Both RRR and $k_F l$ values are widely used to characterize the strength of disorder scattering, and the lower RRR and $k_F l$ values are associated with the stronger disorder scattering. Thus, the above results indicate that the strong disorder scattering is intimately related to the enhancement in superconductivity.

Figs. 1(c) and 1(d) show the field-dependent resistance $R(B)$ at different temperatures of the two samples. When the temperature is much below T_c^{zero} , the superconductivity of the system is inhibited gradually with the increase of the magnetic field, which results to a ‘U’ shape $R(B)$ curve. Near T_c^{zero} the $R(B)$ curve exhibits a ‘V’ shape. Above T_c^{zero} the $R(B)$ curve has a weak dependence on the field. We observe crossing points of the magnetoresistance isotherms occurring at critical magnetic fields near 1.4 T and 0.5 T in the high T_c and low T_c samples, respectively. Furthermore, we

obtain the temperature-dependent resistance at different magnetic fields from Figs. 1(c), 1(d), which is shown in Figs. 1(e), 1(f). We found the high T_c and low T_c samples present different superconductor-metal transition (SMT) behaviors. The low T_c sample shows a normal SMT with monotonic phase boundary separating the regions of $dR/dT > 0$ and $dR/dT < 0$ below and above the critical field around 0.5 T (Fig. 1(f)). For the high T_c sample, when applying magnetic field higher than 1.3 T, the resistance firstly increases with decreasing temperature reaching a maximum around 2.5 K and then decreases at lower temperature. More intriguingly, when the applied magnetic field reaches 1.5 T, the $R(T)$ curve shows a reentrant behavior. Thus the high T_c and low T_c samples exhibit different types of quantum criticality when crossing the critical field.

To thoroughly study the quantum critical behavior, we zoom in the temperature-dependent magnetoresistance near the critical field. We find the $R(B)$ curves of the high T_c sample cross each other in a relatively large transition region instead of a single critical point, as shown in Fig. 2(a). Such a behavior has been ascribed as the fingerprint proof of the QGS [6]. In comparison, the low T_c sample shown in Fig. 2(b) exhibits a much narrower transition region. Figs. 2(c) and 2(d) show the temperature dependence of the crossing magnetic field B_c extracted from the $R(B)$ curves at every two adjacent temperatures. It is obvious that the B_c dependence on the temperature is drastically different between the two samples. B_c of the low T_c sample exhibits an increasing trend with decreasing temperature, complying with the normal QGS behavior [6,8-13,28]. Oppositely, the high T_c sample exhibits an exceptional decreasing trend of B_c with decreasing temperature below T_c , which is ascribed to the anomalous QGS [29]. The normal QGS occurs in the low T_c sample (1.4 K), which is similar to T_c (1.3 K) of the previously reported EuO/KTaO₃ sample with normal QGS [13]. Additionally, we have measured more superconducting samples and reproduced the anomalous QGS in

samples with T_c higher than 1.7 K (Fig. S3).

To analyze the quantum critical phenomenon with series of crossing points, we use the finite-size scaling [30,31] analysis to determine the critical parameter of the two samples. The resistance takes the scaling form $R(B, T) = R_c f[(B - B_c)/T^{1/z\nu}]$, where R_c is the resistance at the crossing field B_c . f is an arbitrary function of B and T with $f[0] = 1$. z is the dynamical critical exponent and ν is the correlation length exponent. The scaling form is rewritten as $R(B, t)/R_c = f[(B - B_c)t]$ with $t = (T/T_0)^{-1/z\nu}$, and t can be obtained by collapsing multiple $R(B, t)$ curves of a single crossing field B_c within a temperature range from T_0 to T . Figs. 3(a)-(d) show representative groups of isothermal curves before and after the data collapsing of the two samples. Fig. 3(a) shows a group of data with $B_c = 1.40$ T and $R_c = 3583 \Omega$ of the high T_c sample in the temperature range from 1.05 K to 1.2 K. After the finite-size scaling the data collapse onto a bivalued curve as shown in Fig. 3(b). The inset of Fig. 3(b) shows the logarithmic dependence of t and T , from which the $z\nu = 12.97$ is obtained in the temperature range of 1.05-1.2 K. Figs. 3(c) and 3(d) show an example of the low T_c sample with similar analysis. The derived dynamical critical exponent $z\nu$ is 1.42 in the temperature range of 0.85-1.1 K. More examples of the analysis in different temperature range can be found in Fig. S4.

The obtained $z\nu$ values in the full temperature range below T_c are shown in Figs. 3(e) and 3(f) for the high and low T_c samples, respectively. As shown in Fig. 3(e), $z\nu$ grows rapidly as temperature decreases and diverges with the temperature approaching zero. The divergent behavior of $z\nu$ can be well described by the activated scaling law $z\nu \propto |B - B_c^*|^{-0.6}$ [6,8] for both samples. It indicates that the infinite-randomness quantum critical point emerges at B_c^* when the temperature approaches zero. In agreement to the anomalous QGS, the crossing magnetic field tends to a minimum B_c^*

of 1.33 T. As for the low T_c sample, $z\nu$ also increases as temperature decreases and diverges with the temperature approaching zero. But the crossing magnetic field approaches a maximum B_c^* of 0.52 T, which agrees to the typical QGS. The above quantitative analyses further confirm the QGS and the anomalous QGS in the low T_c and high T_c samples, respectively.

In Figs. 4(a) and 4(b), we sketch the schematic phase diagram of the high T_c and low T_c samples respectively. Each phase diagram contains regimes of superconducting with vortex lattice, superconducting fluctuation with QGS or anomalous QGS and the normal metal. Strikingly, for the high T_c sample, the strongest superconducting fluctuation appears near T_{BKT} when the quantum fluctuation is competitive with the thermal fluctuation, since the onset critical field (crossing field) B_c reaches the maximum (1.73 T). Below T_{BKT} , the quantum fluctuation overtakes the thermal fluctuation, while B_c decreases with decreasing temperature and approaches 1.33 T at zero temperature. As a result, the superconducting fluctuation regime deeply protrudes into the normal metal regime. Different from the high T_c sample, the low T_c sample exhibits normal-like QGS, which shows that B_c increases with the decreasing temperature, and approaches a maximum of 0.52 T at zero temperature. Nevertheless, relatively weak superconducting fluctuation with a small peak is observed slight above the T_c . For both samples, we derive the upper critical field B_{c2}^{GL} using the Ginzburg-Landau mean field formula [32]. It is found that B_{c2}^{GL} of both samples is close to the quantum critical field B_c^* when the temperature approaches zero. Overall, the phase diagrams demonstrate that the low and high T_c samples exhibit distinctly different quantum fluctuation characters. Especially, the high T_c sample shows the unprecedentedly enhanced quantum fluctuation at a high temperature near T_{BKT} .

Discussion

Although QGS has been found in a number of 2D superconductors with quenched disorders [6,8-13], the anomalous QGS has been rarely discovered. Previously, Y. Liu et al. [29] reported the observation of the anomalous QGS in ultrathin Pb films, which is explained by the effect of pronounced superconducting fluctuations with strong SOC. But the anomalous outward-buckled superconducting phase boundary in the Pb system appears at the temperature far below the T_c , in contrary to the current work. The remarkable difference implies that the disorder and SOC in the LaAlO₃/KTaO₃ system play more profound roles in the superconducting transition. In the close family of the SrTiO₃ and other KTaO₃ based 2DEG superconductors, only normal QGS has been found though both in principle exhibit strong Rashba SOC.

To quantitatively evaluate the strength of Rashba SOC, we perform magnetoresistance measurements in the normal state at 12 K in both samples, and adopt the Maekawa-Fukuyama (MF) model to deduce the SOC parameters [25]. The results are shown in supplementary Fig. S5. It is found that the high T_c sample exhibits a much stronger effective SOC field B_{so} (~ 3.3 T) and Rashba SOC splitting energy Δ_{so} (~ 40.4 meV) than the low T_c sample with $B_{so} \sim 0.9$ T and $\Delta_{so} \sim 22.6$ meV. In addition, the SOC strength can also be estimated in the superconducting state using the equation [25]:

$$B_{c2\parallel}(0K) = \sqrt{\frac{1.76\hbar k_B T_c}{[3\mu_B^2 \tau_{so} + D(d_{sc}e)^2/3]}} \cdot \tau_{so}$$
 is the spin orbit relaxation time ($\Delta_{so} = \hbar/\tau_{so}$). D

is the diffusion constant obtained from the slope of the out of plane upper critical field: $[-d(B_{c2\perp})/dT]_{T=T_c} = 4k_B/\pi D e$. The d_{sc} is the superconducting thickness, which can obtain by comparing $B_{c2\perp}$ and $B_{c2\parallel}$ as shown in Fig. S6. We estimate $B_{c2\parallel}(0K)$ from the measured $B_{c2\parallel}$ at elevated temperatures for both samples using the Ginzburg-Landau model (Figs. S6 and S7). The $B_{c2\parallel}(0K)$ is derived as 19.4 T for the high T_c sample and 6.4 T for the low T_c sample, which are both beyond the

Pauli limit (3.87 T and 2.98 T). Eventually we obtain the τ_{so} and Δ_{so} as 0.012 ps and 57.3 meV for the high T_c sample, and 0.046 ps and 14.2 meV for the low T_c sample. Thus, the high T_c sample indeed exhibits significantly enhanced SOC as compared to the low T_c sample.

Conclusion

In conclusion, the quantum phase transition of the superconducting 2DEG at the LaAlO₃/KTaO₃ interface is systematically studied by the low temperature transport measurements on samples with different disorder scattering strength. The results show that the more disordered sample possesses the higher T_c and stronger Rashba SOC strength. More importantly, we find a crossover of quantum criticality class from the normal QGS in the low T_c sample to the anomalous QGS in the high T_c sample, inseparable from the enhancement of the Rashba SOC. Our findings not only deepen the insight into the exotic quantum criticality of the superconducting LaAlO₃/KTaO₃ interface, but also open a new frontier of researches in disorder-tuned or SOC-enriched quantum phase transitions in 2D superconductors.

Acknowledgement

The work was financially supported by National Key R&D Program of China (Nos. 2022YFA1403000, 2023YFA1406301), the National Science Foundation of China (Nos. 12104305, 52072244). The research used resources from Analytical Instrumentation Center (#SPST-AIC10112914) and Soft Matter Nanofab (SMN180827) in ShanghaiTech University.

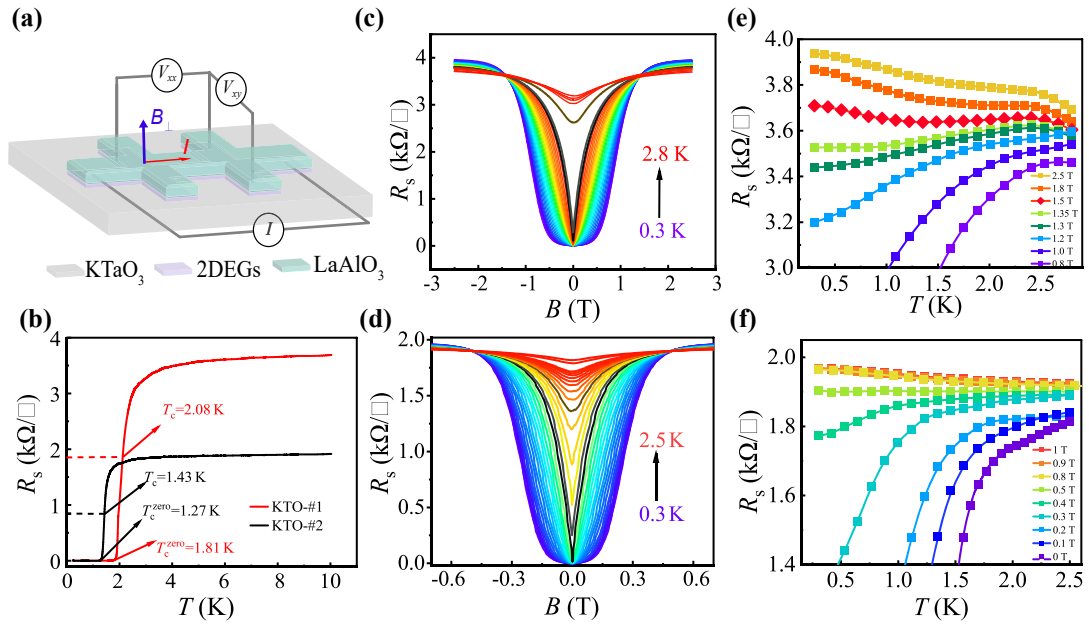


FIG.1 Transport measurements for LaAlO₃/KTaO₃ (111) samples. (a) Schematic of the Hall bar device and the measurement geometry. (b) Temperature-dependent sheet resistance below 10 K under zero magnetic field. T_c^{zero} and T_c (defined as $R(T_c) = 0.5 \times R(10 \text{ K})$) are indicated by red arrows for Sample labeled as KTO-#1 and black arrows for Sample labeled as KTO-#2, respectively. The isotherm $R(B)$ curves measured at different temperatures of (c) KTO-#1 and (d) KTO-#2. The isomagnetic $R(T)$ curves measured under various perpendicular magnetic fields of (e) Sample KTO-#1 and (f) Sample KTO-#2. The superconducting reentrant behavior in Sample KTO-#1 is highlighted with the red diamond symbols.

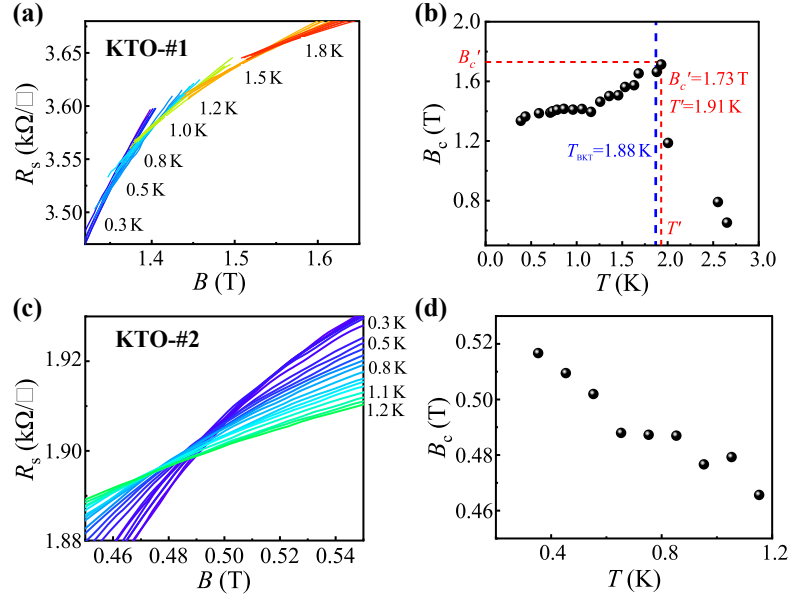


FIG.2 Anomalous QGS and normal QGS behaviors. (a) The crossing region of isotherms $R(B)$ curves of KTO-#1 from 0.3 K to 2.8 K. (b) The temperature dependence of crossing point B_c of every two adjacent $R(B)$ curves deduced from (a). (c) The crossing region of isothermal $R(B)$ curves of KTO-#2 from 0.3 K to 1.2 K. (d) The temperature dependence of crossing point B_c of every two adjacent $R(B)$ curves deduced from (c).

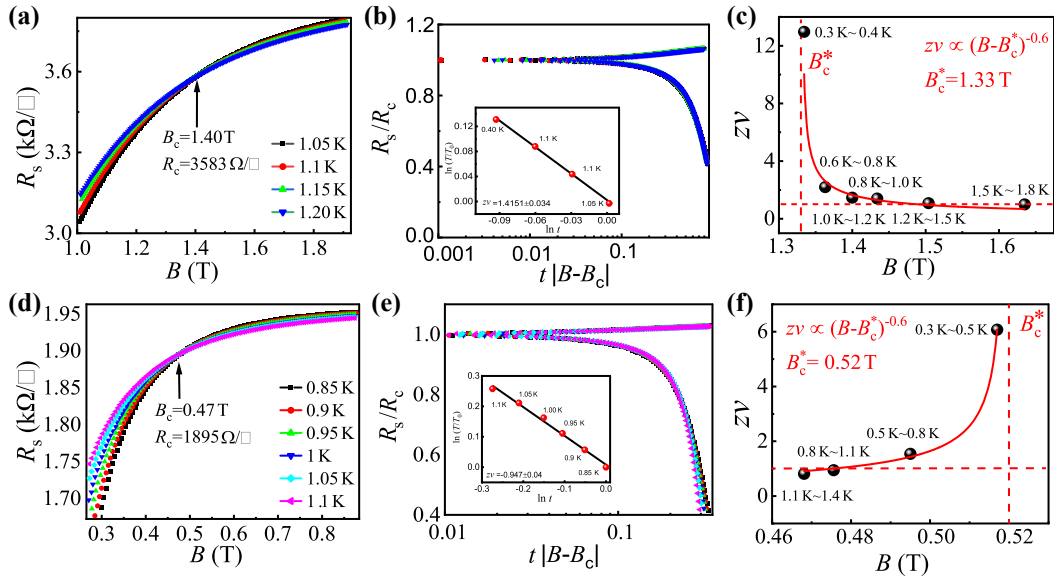


FIG.3 The Finite-size scaling analysis of representative groups for both samples with the anomalous QGS and normal QGS behaviors. (a-d) The isothermal $R(B)$ curves of (a) KTO-#1 in the temperature range of 1.05-1.2 K and (c) KTO-#2 in the temperature range of 0.85-1.1 K. (b), (d) The corresponding normalized sheet resistance of (a) and (c) as a function of $t|B_c - B|$, where $t = (T/T_0)^{-1/z\nu}$. The insets show the linear fitting between $\ln(T/T_0)$ and $\ln t$. The $z\nu$ values are obtained from the slopes of the fitting lines. (e),(f) The divergent behavior of $z\nu$ with temperature approaching zero and magnetic field tending to (e) a minimal B_c^* in KTO-#1 corresponding to anomalous QGS and (f) a maximal B_c^* in KTO-#2 corresponding to normal QGS. B_c^* is deduced from the activated scaling law $z\nu \propto |B - B_c^*|^{-0.6}$.

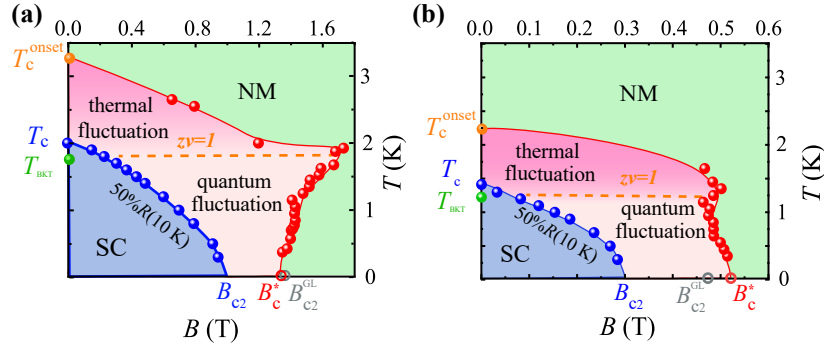


FIG.4 The Phase diagram for (a) the high T_c sample with anomalous QGS and (b) the low T_c sample with normal-like QGS, respectively. The plots are based on the transport data. Red spheres and blue spheres represent the crossing points B_c of the isothermal $R(B)$ curves and the upper critical magnetic field B_{c2} . The orange sphere indicates the onset temperature of superconducting transition with $R(T_c^{\text{onset}}) = 0.9 \times R(10 \text{ K})$. The red hollow indicates the infinite-randomness quantum critical point B_c^* at zero temperature. The gray hollow indicates B_c^{GL} extrapolated from the Ginzburg-Landau formula. SC and NM represent superconducting state and normal metal, respectively. When $z\nu > 1$, thermal fluctuation dominates the phase transition; when $z\nu < 1$, quantum fluctuation takes over. In both diagrams, the division line $z\nu = 1$ is found at T_{BKT} .

- [1] L. Fu and C. L. Kane, *Phys. Rev. Lett.* **100**, 096407 (2007).
- [2] Z. Chen, B. Y. Wang, A. G. Swartz, H. Yoon, Y. Hikita, S. Raghu, and H. Y. Hwang, *npj Quantum Mater.* **6**, 15 (2021).
- [3] A. Tsen, B. Hunt, Y. Kim, Z. Yuan, S. Jia, R. Cava, J. Hone, P. Kim, C. Dean, and A. Pasupathy, *Nat. Phys.* **12**, 208 (2016).
- [4] D. Sherman, U. S. Pracht, B. Gorshunov, S. Poran, J. Jesudasan, M. Chand, P. Raychaudhuri, M. Swanson, N. Trivedi, A. Auerbach, M. Scheffler, A. Frydman, and M. Dressel, *Nat. Phys.* **11**, 188 (2015).
- [5] M.-A. Méasson, Y. Gallais, M. Cazayous, B. Clair, P. Rodiere, L. Cario, and A. Sacuto, *Phys. Rev. B* **89**, 060503 (2014).
- [6] Y. Xing, H. Zhang, H. Fu, H. Liu, Y. Sun, J. Peng, F. Wang, X. Lin, X. Ma, Q. Xue, Jian Wang, and X. C. Xie, *Science* **350**, 542 (2015).
- [7] R. B. Griffiths, *Phys. Rev. Lett.* **23**, 17 (1969).
- [8] C. Huang, E. Zhang, Y. Zhang, J. Zhang, F. Xiu, H. Liu, X. Xie, L. Ai, Y. Yang, M. Zhao, J. Qi, L. Li, S. Liu, Z. Li, R. Zhan, Y. Q. Bie, X. Kou, S. Deng, and X. C. Xie, *Sci. Bull.* **66**, 1830 (2021).
- [9] N. A. Lewellyn, I. M. Percher, J. Nelson, J. Garcia-Barriocanal, I. Volotsenko, A. Frydman, T. Vojta, and A. M. Goldman, *Phys. Rev. B* **99**, 054515 (2019).
- [10] Q. Zhao, T. N. Shao, W. L. Yang, X. Y. Wang, X. Y. Chen, M. H. Chen, F. H. Zhu, C. X. Chen, R. F. Dou, C. M. Xiong, H. Liu, and J. C. Nie, *Phys. Rev. Lett.* **133**, 036003 (2024).
- [11] S. Yadav, M. P. Saravanan, and S. Sahoo, *Commun. Phys.* **7** (2024).
- [12] S. C. Shen, Y. Xing, P. J. Wang, H. W. Liu, H. L. Fu, Y. W. Zhang, L. He, X. C. Xie, X. Lin, J. C. Nie, and J. Wang, *Phys. Rev. B* **94**, 144517 (2016).
- [13] Y. Ma, J. Niu, W. Xing, Y. Yao, R. Cai, J. Sun, X. Xie, X. Lin, and W. Han, *Chinese Phys. Lett.* **37**, 117401 (2020).
- [14] T. Moriya and K. Ueda, *Adv. Phys.* **49**, 555 (2000).
- [15] B. Michon, C. Girod, S. Badoux, J. Kacmarcik, Q. Ma, M. Dragomir, H. A. Dabkowska, B. D. Gaulin, J. S. Zhou, S. Pyon, T. Takayama, H. Takagi, S. Verret, N. Doiron-Leyraud, C. Marcenat, L. Taillefer, and T. Klein, *Nature* **567**, 218 (2019).
- [16] M. Frachet, I. Vinograd, R. Zhou, S. Benhabib, S. F. Wu, H. Mayaffre, S. Krämer, S. K. Ramakrishna, A. P. Reyes, J. Debray, T. Kurosawa, N. Momono, M. Oda, S. Komiya, S. Ono, M. Horio, J. Chang, C. Proust, D. LeBoeuf, and M. H. Julien, *Nat. Phys.* **16**, 1064 (2020).
- [17] P. Gegenwart, Q. Si, and F. Steglich, *Nat. Phys.* **4**, 186 (2008).
- [18] P. Walmsley, C. Putzke, L. Malone, I. Guillamon, D. Vignolles, C. Proust, S. Badoux, A. I. Coldea, M. D. Watson, S. Kasahara, Y. Mizukami, T. Shibauchi, Y. Matsuda, and A. Carrington, *Phys. Rev. Lett.* **110**, 257002 (2013).
- [19] A. Ohtomo and H. Hwang, *Nature* **427**, 423 (2004).
- [20] A. Caviglia, S. Gariglio, N. Reyren, D. Jaccard, T. Schneider, M. Gabay, S. Thiel, G. Hammerl, J. Mannhart, and J.-M. Triscone, *Nature* **456**, 624 (2008).
- [21] C. Liu, X. Yan, D. Jin, Y. Ma, H. Zhou, H.-W. Hsiao, A. Bhattacharya, Y. Lin, X. Zhou, J. Pearson, B. Fisher, J. S. Jiang, W. Han, D. D. Fong, J. Sun, Jian-Min Zuo, Terence M. Bretz-Sullivan, and Jianguo Wen, *Science* **371**, 716 (2021).

- [22] Z. Chen, Y. Liu, H. Zhang, Z. Liu, H. Tian, Y. Sun, M. Zhang, Y. Zhou, J. Sun, and Y. Xie, *Science* **372**, 721 (2021).
- [23] V. Kozii and L. Fu, *Phys. Rev. Lett.* **115**, 207002 (2015).
- [24] G. Zhang, L. Wang, J. Wang, G. Li, G. Huang, G. Yang, H. Xue, Z. Ning, Y. Wu, J. P. Xu, Y. Song, Z. An, C. Zheng, J. Shen, J. Li, Y. Chen, and W. Li, *Nat. Commun.* **14**, 3046 (2023).
- [25] X. Hua, F. Meng, Z. Huang, Z. Li, S. Wang, B. Ge, Z. Xiang, and X. Chen, *npj Quantum Mater.* **7**, 97 (2022).
- [26] X. Chen, T. Yu, Y. Liu, Y. Sun, M. Lei, N. Guo, Y. Fan, X. Sun, M. Zhang, F. Alarab, V. Strocov, Y. Wang, T. Zhou, X. Liu, F. Lu, W. Liu, Y. Xie, R. Peng, H. Xu, and D. Feng, *Nat. Commun.* **15**, 7704 (2024).
- [27] Z. Chen, Z. Liu, Y. Sun, X. Chen, Y. Liu, H. Zhang, H. Li, M. Zhang, S. Hong, T. Ren, C. Zhang, H. Tian, Y. Zhou, J. Sun, and Y. Xie, *Phys. Rev. Lett.* **126**, 026802 (2021).
- [28] F. Chen, Y. Liu, W. Guo, T. Wang, Z. Tian, M. Zhang, Z. Xue, G. Mu, X. Zhang, and Z. Di, *Nano Lett.*, 24 (2024).
- [29] Y. Liu, Z. Wang, P. Shan, Y. Tang, C. Liu, C. Chen, Y. Xing, Q. Wang, H. Liu, X. Lin, X. C. Xie, and J. Wang, *Nat. Commun.* **10** (2019).
- [30] M. P. Fisher, *Phys. Rev. Lett.* **65**, 923 (1990).
- [31] S. L. Sondhi, S. Girvin, J. Carini, and D. Shahar, *Rev. Mod. Phys.* **69**, 315 (1997).
- [32] Y. Saito, Y. Kasahara, J. Ye, Y. Iwasa, and T. Nojima, *Science* **350**, 409 (2015).

Supplemental Material for

Observation of Quantum Criticality Class Crossover at the

LaAlO₃/KTaO₃ (111) Interface

Jia Liu,^{1,*} Long Cheng,^{1,*†} Junkun Zha,^{1,2} Fei Ye,¹ Xiaofang Zhai^{1,†}

¹ School of Physical Science and Technology, Shanghai Tech University, Pudong, Shanghai 201210, China.

² Department of Physics, University of Science and Technology of China, Hefei, Anhui 230026, China

* These authors contributed equally to this work.

† Corresponding authors: chenglong1@shanghaitech.edu.cn, zhaixf@shanghaitech.edu.cn.

This file includes

Methods

Figs. S1-S7

Table. S1

Methods

Sample preparation

The KTaO_3 (111) substrates were annealed in a tube furnace for 2 h at 650°C , followed by the water bath at 60°C for 30 min. Finally, an atomically flat surface with Ta-rich termination was obtained. Then $\text{LaAlO}_3/\text{KTaO}_3$ (111) samples were prepared by depositing the LaAlO_3 thin films on the treated KTaO_3 (111) substrate using pulsed laser deposition (PLD). The sample properties can be controlled by the growth condition. The detail growth conditions of the samples in this work are as follows: the growth temperature of the high T_c sample (KTO-#1) was 400°C and that of the low T_c sample (KTO-#2) was 250°C . The oxygen pressure was 5×10^{-5} Pa. The LaAlO_3 target was ablated with a 248 nm KrF excimer laser at a repetition frequency of 2 Hz. The laser energy density was about 0.9 J cm^{-2} . The LaAlO_3 thicknesses of all samples were kept the same at about 10 nm with the growth rate calibrated through the X-ray reflectivity (XRR) method. To protect the sample from being oxidized in the air, an additional 20 nm LaAlO_3 capping layer was deposited at the oxygen pressure of 6 Pa.

Hall bar patterns were fabricated by UV lithography with the ML3 Aligner. Firstly, the photoresist was patterned into Hall bar on the bare KTaO_3 substrate. Next, a 20 nm LaAlO_3 layer was deposited at the oxygen pressure of 6 Pa as a hard mask. After the lift-off process, an active Hall bar region of the uncovered KTaO_3 substrate was obtained. With the following deposition of the LaAlO_3 film at the oxygen pressure of 5×10^{-5} Pa, the Hall-bar-shaped 2DEG was consequently formed. The channel width and length of the Hall bar was 100 μm and 250 μm , respectively.

Transport measurement

The contacts to the $\text{LaAlO}_3/\text{KTaO}_3$ interfacial 2DEG were ultrasonically bonded with Al wires. The transport measurements were carried out in a commercial physical

property measurement system (PPMS) with the temperature range of 2-300 K and the magnetic field up to 9 T. The ultralow-temperature measurements from 0.3 K to 10 K were measured in the Oxford He³ cryostat with the AC technique, using the 0.5 μ A excitation current at 13.567 Hz and the 0.15 T/min field sweeping rate.

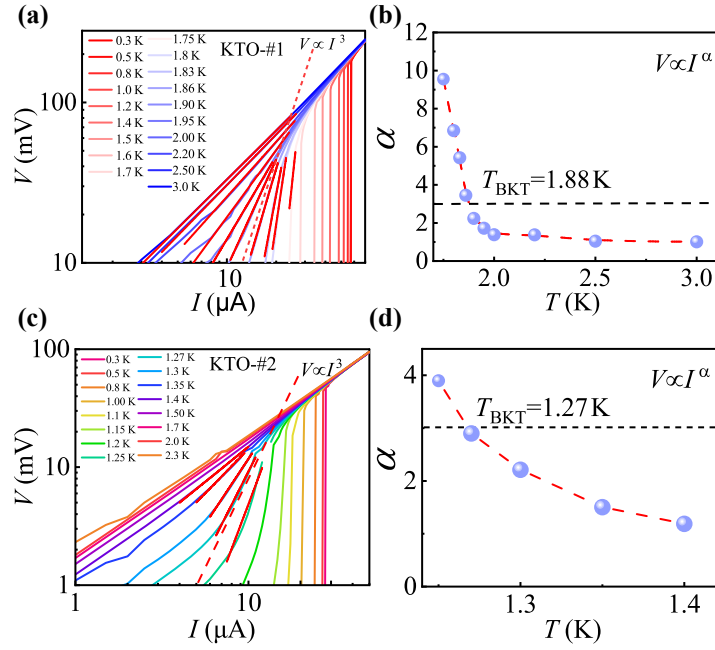


Fig. S1. Current-voltage behavior of (a) KTO-#1 and (c) KTO-#2. I - V curves measured at different temperatures are plotted in a logarithmic-logarithmic scale. The red dashed line represents the relation of $V \propto I^3$, which is used to determine the BKT transition temperature T_{BKT} . The temperature dependence of the power-law exponent α ($V \propto I^\alpha$) for (b) KTO-#1 and (d) KTO-#2 derived from (a) and (c), respectively.

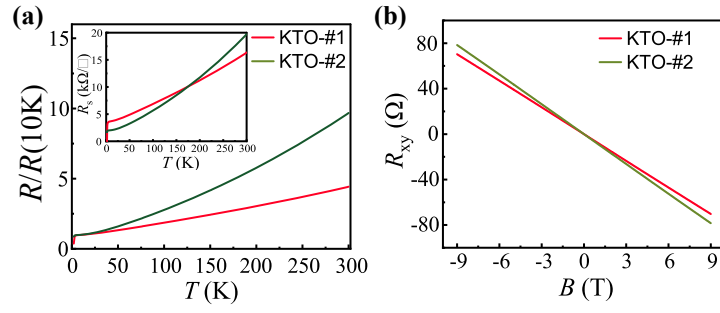


Fig. S2. (a) The normalized sheet resistance $R/R(10\text{ K})$ as a function of the temperature in a wide range from 2K to 300K for both samples. The inset shows the original temperature-dependent sheet resistance. (b) Hall resistance as a function of magnetic field measured at 12K. The transport parameters for both samples, including carrier density, mobility, mean free path and so on, are summarized in Table S1.

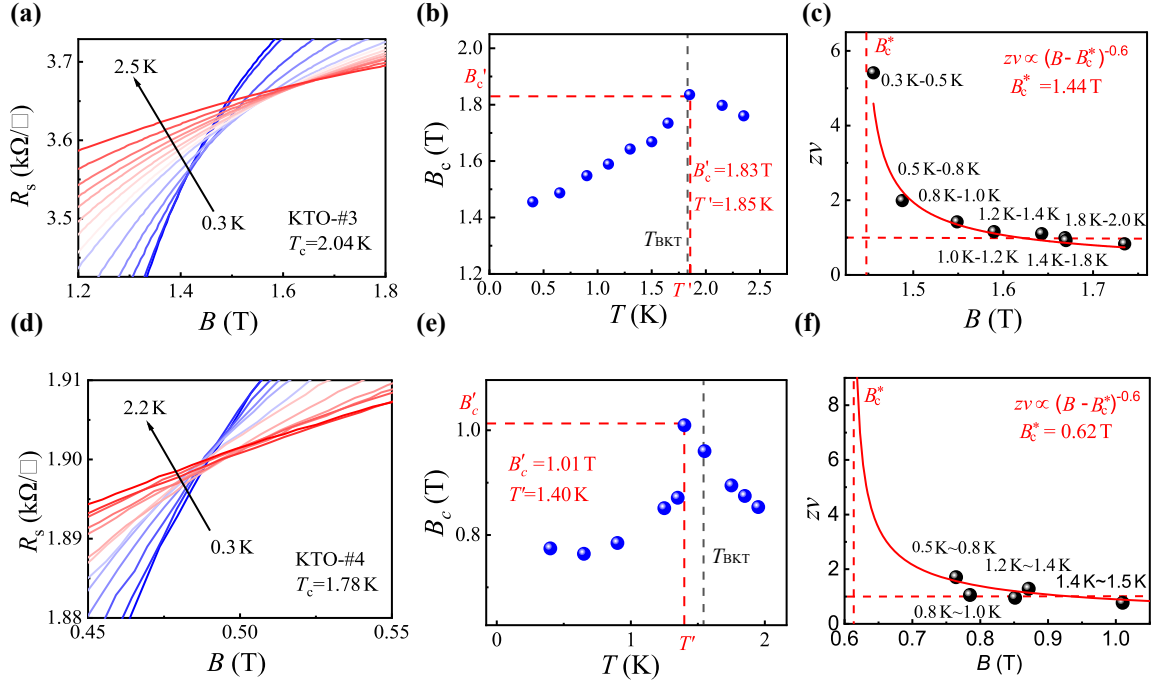


Fig. S3. The anomalous QGS phenomenon reproduced in other $\text{LaAlO}_3/\text{KTaO}_3$ samples.

The isothermal $R(B)$ curves at different temperatures of (a) a $\text{LaAlO}_3/\text{KTaO}_3$ sample with $T_c = 2.04$ K and (b) another one with $T_c = 1.78$ K. (c)(d) The temperature dependence of crossing point B_c of every two adjacent $R(B)$ curves deduced from (a) and (b) respectively. (e)(f) The divergent behavior of $z\nu$ with temperature approaching zero and magnetic field tending to (e) a minimal B_c^* , which indicates the anomalous QGS.

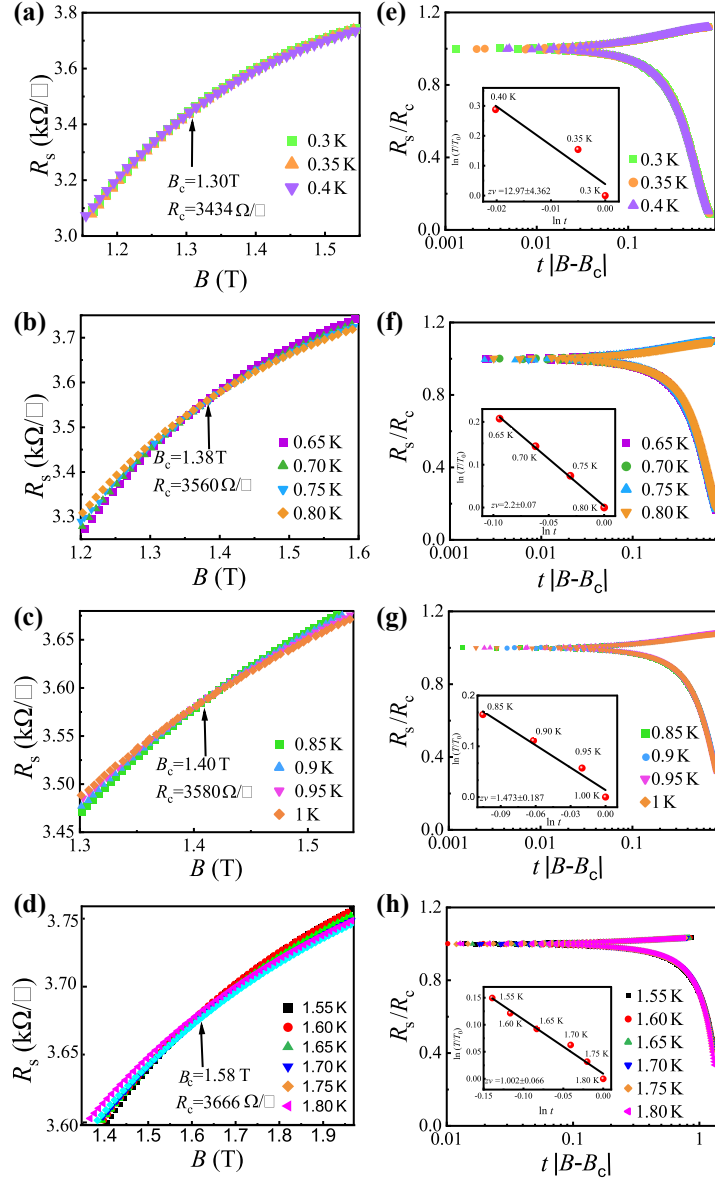


Fig. S4. Finite-size scaling analysis for KTO-#1 at temperatures from 0.3 K to 1.8 K.

(a-d) The isothermal $R(B)$ curves in the temperature ranges of (a) 0.3-0.5 K, (b) 0.65-0.8 K, (c) 0.85-1 K and (d) 1.55-1.8 K. (e-h) Corresponding normalized sheet resistances as a function of scaling variable $(B - B_c)t$, with $t = (T/T_0)^{-1/z\nu}$. The insets are the linear fittings between $\ln(T/T_0)$ and $\ln(t)$, which give the values of the critical exponent $z\nu$.

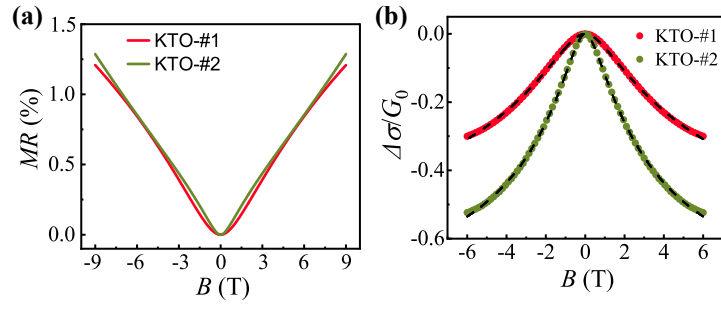


Fig. S5. (a) The magnetoresistance behavior of both samples measured at 12K. (b) Weak antilocalization analysis of both samples. Black dashed lines are the fittings of magnetoconductances with Maekawa-Fukuyama formula for both samples. The derived effective SOC field B_{so} is ~ 3.3 T and ~ 0.9 T, while the Rashba SOC splitting energy Δ_{so} is ~ 40.4 meV and ~ 22.6 meV for KTO-#1 and KTO-#2, respectively.

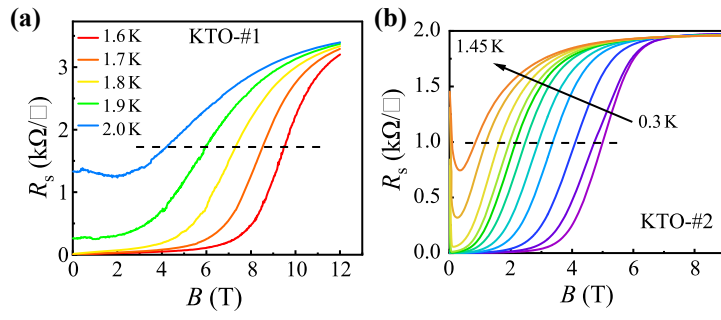


Fig. S6. (a) The temperature-dependent $R(B)$ curves under the in-plane magnetic fields at the temperature range of 1.6-2.0 K for KTO-#1. (b) The temperature-dependent $R(B)$ curves under the in-plane magnetic fields at the temperature range of 0.3-1.45 K for KTO-#2. The black dashed line indicates half of the normal state resistance $R_{(10\text{ K})}$.

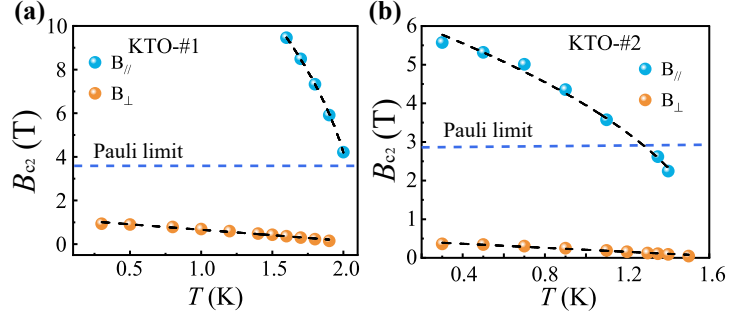


Fig. S7. Temperature dependence of the critical field for (a) KTO-#1 and (b) KTO-#2 under magnetic fields perpendicular and parallel to the interface. These data (symbols) were determined at half of $R(10\text{ K})$ from Fig. 1 and Fig. S4. They can be fitted with the phenomenological Ginzburg-Landau theory. For the perpendicular field B_{\perp} , it yields a linearized equation at the near-critical temperatures ($(T_c - T)/T_c \ll 1$): $B_{c\perp}(T) = \phi_0(1 - T/T_c)/[2\pi(\xi_{\text{GL}})^2]$, where ϕ_0 is magnetic flux quantum and ξ_{GL} is the coherence length at $T=0\text{ K}$. For the parallel field B_{\parallel} , the 2D Ginzburg-Landau yields a square-root equation: $B_{c2\parallel}(T) = \phi_0\sqrt{(1 - T/T_c)}/[2\pi\xi_{\text{GL}}d_{\text{sc}}]$, where d_{sc} is the effective thickness of superconductivity. Combine $B_{c\perp}(0)$ and $B_{c2\parallel}(0)$, we can obtain ξ_{GL} and d_{sc} of both samples as shown in Table. S1. The gray dashed line indicates the Pauli paramagnetic limit, which is 3.87 T and 2.98 T for KTO-#1 and KTO-#2 respectively.

Table S1. Summary of transport parameters for both samples.

Sample	n_{2D} (cm^{-2})	μ ($\text{cm}^2\text{V}^{-1}\text{s}^{-1}$)	k_F (nm^{-1})	l (nm)	ξ_{GL} (nm)	$k_F l$	RRR
KTO-#1	8.0×10^{13}	53	2.24	7.7	15.5	17.3	4.4
KTO-#2	6.7×10^{13}	113	2.12	15.8	24.2	33.4	9.7